

Lawrence Berkeley National Laboratory

LBL Publications

Title

Ultrafast Hot Carrier Injection in Au/GaN: The Role of Band Bending and the Interface Band Structure

Permalink

<https://escholarship.org/uc/item/1880683p>

Journal

The Journal of Physical Chemistry Letters, 10(20)

ISSN

1948-7185

Authors

Zheng, Fan

Wang, Lin-Wang

Publication Date

2019-10-17

DOI

10.1021/acs.jpcllett.9b02402

Supplemental Material

<https://escholarship.org/uc/item/1880683p#supplemental>

Peer reviewed

Ultrafast hot carrier injection in Au/GaN: the role of band bending and the interface band structure

Fan Zheng and Lin-wang Wang*

Joint Center for Artificial Photosynthesis and Materials Sciences Division, Lawrence Berkeley National Laboratory, Berkeley, California 94720, USA.

E-mail: lwwang@lbl.gov

Abstract

Plasmon photochemistry can potentially play a significant role in photocatalysis. To realize this potential, it is critical to enhance the plasmon excited hot carrier transfer and collection. However, the lack of atomistic understanding of the carrier transfer across the interface, especially when the carrier is still “hot”, makes it challenging to design more efficient system. In this work, we apply the non-adiabatic molecular dynamics simulation to study hot carrier dynamics in the system of Au nanocluster on top of GaN surface. By setting up the initial excited hole in Au, the carrier transfer from Au to GaN is found to be on a sub-pico second time scale. The hot hole first cools to the band edge of Au *d*-states while it transfers to GaN. After the hole has cooled down to the band edge of GaN, we find some of the charges can return back to Au. By applying different external potentials to mimic the Schottky-barrier band bending, the returning charge can be reduced, demonstrating the importance of the internal electric field. Finally, with the understanding of the carrier transfer’s pathway, we suggest

16 that a ZnO layer between GaN and Au can effectively block the “cold” carrier from
17 returning back to Au but still allow the hot carrier to transfer from Au to GaN.

18 Photochemistry relies on photo generated carriers to execute electrochemical reactions.
19 Recently, plasmon has been used as a potential photo absorber to generate photo carriers.¹⁻⁴
20 Due to the involvement of many electrons in a plasmon excitation, the plasmon mode in a
21 metal nano-system can have much higher optical oscillator strength than a typical semicon-
22 ductor, thus it has higher light absorbing efficiency. It has also been shown recently that
23 the collective many-particle plasmon excitation can convert its energy into single-particle
24 excitation inside the metal nano-system within 100 fs .^{2,5} One way to harvest such single
25 particle hot carrier is to attach the metal nano-system (e.g., a metallic quantum dot, QD)
26 to a semiconductor substrate. In this case, the hot carrier cooling process is accompanied by
27 carrier injection and carrier transfer into semiconductor substrates. Questions arise for the
28 carrier injection process: (1) what determines the competition between the carrier cooling
29 inside the metal-QD and the carrier injection into the substrate? (2) Can the substrate
30 harvest hot carrier instead of equilibrium ones (“cold” carrier) at the band edge, which
31 can be used to drive the hot carrier nonequilibrium reaction? (3) What is the typical time
32 scale for cooling and carrier injection? (4) How the interface electronic structure and band
33 alignment influence the hot carrier injection? Answering these questions are important. For
34 example, a lot of recent effort has been placed to study the possibility of hot carrier catal-
35 ysis in various redox reactions such as water splitting and oxidation,⁶⁻¹¹ H₂ decomposition
36 or production,¹²⁻¹⁴ and CO₂ reduction.¹⁵⁻¹⁷ Thus, designing an efficient way to harvest hot
37 carriers (not just the “cold” carrier) becomes an important research topic.

38 The reported efficiencies of the plasmon assisted catalytical reactions are generally low.¹⁸⁻²¹
39 Less than 3% solar-to-chemical efficiency is obtained in CsS-Au-TiO₂ sandwich system,¹⁸
40 which is far below the solar cell light conversion efficiency. In an Au/TiO₂ system, the effi-
41 ciency of the light induced carrier transferred is only 0.2%.²¹ It is possible that only a small
42 portion of hot carriers has been injected into the carrier collection material during their
43 cooling. The transient pump-probe experiments using absorption spectroscopy or non-linear
44 optics techniques show that the time scale of the charge transfer from a quantum dot or

45 metal cluster to a semiconductor is on the order of sub-pico second.^{22–28} However, the exact
46 pictures of such carrier injection and carrier cooling processes are difficult to probe experi-
47 mentally. To understand such process in the atomic scale, theoretical simulation has been
48 used to study this process.^{29–33} For example, Atwater et al estimate the surface plasmon
49 decay rate and the initial hot-carrier distribution in metals using Fermi’s golden rule.^{29,30}
50 The carrier transport is then evaluated by first-principle method based on electron-electron
51 and electron-phonon scattering. Bernardi and Zhou use perturbation method to compute the
52 electron-phonon coupling.^{32,33} Combining with the Boltzmann equation, the carrier mobility
53 and carrier cooling process are revealed in the bulk system. While such methods are excellent
54 in studying bulk systems or interface scattering of large systems, it is not a direct simulation
55 of a nano hetero-system as a whole. Thus, it might be difficult to study the carrier injection
56 in a heterogeneous nano-system. Another analytical approach to study carrier injection is
57 to calculate charge transfer rate with formula like the Marcus theory.^{34–38} However, such
58 calculations can only reveal charge transfer for localized carriers and for equilibrium cold
59 carriers instead of hot carriers.

60 One alternative approach is to simulate the hot carrier cooling and injection directly using
61 nonadiabatic electronic dynamics. In this approach, the time-dependent Schrödinger’s equa-
62 tion is followed to directly simulate the change of carrier wavefunction. It is suitable to study
63 nano-systems with about one hundred atoms, thus it is complementary to the analytical stud-
64 ies based on bulk behaviors.^{29,30} Pioneer works based on non-adiabatic molecular dynamics
65 or time-dependent density function theory have studied the carrier motion for interfacial sys-
66 tems, such as Dye-sensitized TiO₂,^{39,40} Ag (and Au) on MoS₂,⁴¹ Au nanoparticle/nanorod
67 on TiO₂,^{42,43} PbSe nanoparticle on TiO₂,⁴⁴ bilayer two-dimension heterostructures,⁴⁵ and
68 graphene on TiO₂.⁴⁶ They all demonstrate the fast carrier transfer within a few hundreds
69 femtosecond across the interface. However, most of these works illustrate the details of
70 the electron transfer from the band edge of a quantum dot, semiconductor or dye to an-
71 other semiconductor.^{39,40,44} Some other works also demonstrate the delocalization across the

72 metal/semiconductor interface from a plasmon-like adiabatic state near the Fermi level.^{42,45}
73 However, in most cases, the transferred carriers are band edge carrier, instead of hot carriers.
74 There are not enough studies of the hot carrier cooling in combination of charge transfer. On
75 the other hand, many works^{43,47-49} use nonadiabatic molecular dynamics to study hot carrier
76 cooling (e.g. inside a QD), but no injection process. Thus, there is a lack of study to reveal
77 the competition between hot carrier's cooling and hot carrier injection, and different path-
78 ways for hot carrier injections. Furthermore, although Schottky barrier and its related band
79 bending exist in almost all the metal-semiconductor interfaces, a detailed understanding for
80 the role of the Schottky barrier to the carrier transfer is also lacking.

81 In this work, inspired by the recent experimental work of Au nanocluster on GaN for
82 the plasmon hot carrier injection,¹⁶ we use the non-adiabatic molecular dynamics (NAMD)
83 to reveal the details of the hot carrier's cooling and its injection from the Au metal to the
84 GaN substrate. Our NAMD is based on a newly developed algorithm called P-matrix for-
85 malism.^{50,51} Unlike previous NAMD methods where multi-trajectory stochastic simulations
86 are used to represent the ensemble of the trajectories to include the detailed balance and
87 decoherence effect,^{40-42,44-46} in our P-matrix formalism, a single run can represent a whole en-
88 semble result while including the detailed balance and decoherence effect. In this formalism,
89 the decoherence can be introduced naturally, and detailed balance is also satisfied. The effi-
90 ciency of this new algorithm allows us to study various situations for relatively large systems
91 and relatively long simulation times. By studying the detailed process of the hot carrier's
92 pathway, different sizes of the system, different strength of the applied electric field, and
93 addition of a hole-blocking layer, our simulation reveals the competitions between different
94 relaxation channels, and finds a surprising result of fast carrier injection from Au nanocluster
95 to GaN substrate before the carrier cooling down. After arriving at GaN band edge, some
96 carriers return back to Au nanocluster. Such detailed picture of the hot carrier transfer can
97 help us design more efficient systems to enhance the hot carrier injection efficiency.

98 In our NAMD simulation, we first perform a density functional theory (DFT) ground state

99 Born-Oppenheimer molecular dynamics (BOMD) simulation. Its nuclear trajectory and the
100 time-dependent Hamiltonian $\mathbf{H}(t)$ is then used to carry out the time evolution of the wave
101 function following the time-dependent Schrödinger's equation: $i\partial\psi(t)/\partial t = \mathbf{H}(t)\psi(t)$. Differ-
102 ent from other NAMD methods, the time-dependent Schrodinger's equation is reformulated
103 following the P-matrix equation in a density matrix formalism.⁵⁰ In this way, it is possible to
104 take into account the detailed balance and decoherence effect at the same time. The detailed
105 balance is important in order to describe the cooling process, while the decoherence (dephas-
106 ing) also influences the cooling rate. In this approach, we have ignored the back reaction
107 from the electron movement to the nuclear movement. This approximation is also called
108 classical path approximation (CPA) which are widely used in other NAMD methods.^{40,41,45}
109 Such CPA is appropriate for relatively large systems when hot carriers not highly localized,
110 thus the back reaction from the electron movement to the nuclear movement is negligible,
111 and the main interest of study is at the electron dynamics, not the nuclear dynamics.

112 We perform the plane-wave pseudopotential DFT calculation implemented in PWmat
113 package^{52,53} with the generalized gradient approximation (GGA) exchange correlation func-
114 tional.⁵⁴ The atomic structure is relaxed prior to molecular dynamics (MD) simulations, and
115 SG15 pseudopotentials⁵⁵ are used with 50 Ryd plane wave kinetic energy cutoff. Here, the
116 pseudopotential of Au has been modified so that the position of d -orbitals in terms of the
117 Fermi level are consistent to the experiment⁵⁶ (see Supplementary Information (SI)). Al-
118 though DFT tends to underestimate work function and ionization energy for Au nanocluster
119 and GaN surface, respectively, we find that their energy level difference for Au and GaN
120 calculated by DFT is quite consistent with the experiments.⁵⁷⁻⁶⁰ Therefore, the work func-
121 tion and ionization energy are not corrected here (see SI). Fig. 1a shows the system we have
122 constructed. The non-polar surfaces $[11\bar{2}0]$ of GaN attaching the Au nanocluster is used
123 to avoid surface reconstruction.⁶¹ The Au nanocluster with 30 Au atoms is obtained via a
124 simulated annealing using *ab initio* MD where the temperature is initially increased up to
125 1100 K and then cooled down slowly. A relaxation of the whole system is then performed

126 to reduce forces on all the atoms to be below $0.02 \text{ eV}/\text{\AA}$. The calculated density of states is
 127 shown in Fig. 1b, where the Fermi level of Au is within the band gap of GaN. Our previous
 128 work has demonstrated that the hot carrier can be obtained in d -states within 50 fs upon
 129 the excitation of the plasmon in Ag_{55} nanocluster.⁵ In this work, we set up initial hot holes
 130 at various d -states of Au nanocluster and perform NAMD to investigate their dynamics.

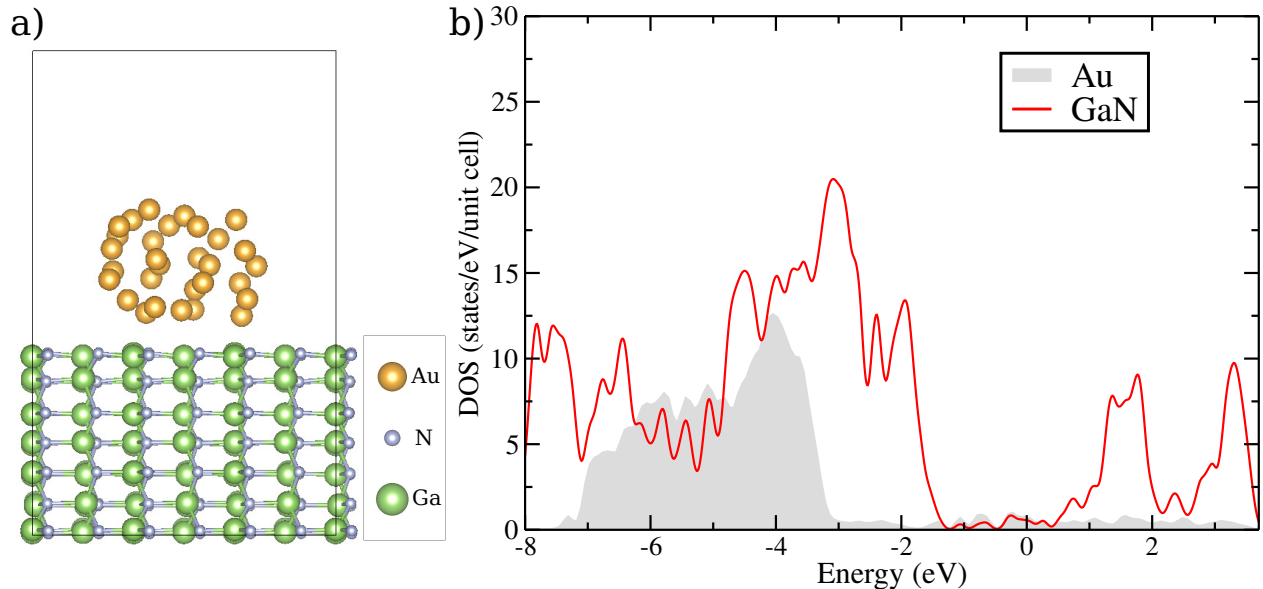


Figure 1: a) Structure of Au/GaN system under simulation (relaxed at 0K). It has 30 Au atoms and 252 GaN atoms. b) Density of states of the 0K structure projected to GaN and Au, respectively. Fermi energy is set at energy 0 eV.

131 In our NAMD simulation, the system is firstly simulated with a Born-Oppenheimer elec-
 132 tronic ground state molecular dynamics (BOMD) at room temperature (300K). Then the
 133 evaluation of the carrier wavefunction is done as a post-process. The hot-carrier wavefunction
 134 $\psi_l(t)$ is evolved following the Schrödinger's equation, and it is expanded with the adiabatic
 135 basis $\phi_i(t)$ as $\psi_l(t) = \sum_i C_i^l \phi_i(t)$. Using the density matrix formalism, the density matrix of
 136 the system is $D_{ij}(t) = \sum_l w_l C_i^{l*}(t) C_j^l(t)$, under the basis of $\phi_i(t)$, where w_l is the weight of ψ_l .
 137 Due to this w_l , a $D_{ij}(t)$ can represent an ensemble of wavefunction trajectories. Following
 138 the time-dependent Schrödinger's equation, the equation of motion for the density matrix
 139 can be written down as:⁵⁰

$$\frac{\partial}{\partial t} D_{ij}(t) = -i [V(t), D(t)]_{ij} - (1 - \delta_{ij}) \frac{D_{ij}(t)}{\tau_{ij}(t)} \quad (1)$$

140 and $V_{ij}(t) = \delta_{ij}\epsilon_i(t) - i \langle \phi_i(t) | \partial \phi_j(t) / \partial t \rangle$ contains the information of the change of adiabatic
 141 state $\phi_i(t)$, which implicitly includes the effect of the electron-phonon coupling. The second
 142 term is used to introduce the decoherence where $\tau_{ij}(t)$ represents the decoherence time
 143 between state i and j . To introduce the detailed balance, a P-matrix formalism is used
 144 where the density matrix \mathbf{D} is splitted into $\mathbf{D} = \mathbf{P} + \mathbf{P}^T$ with P_{ij} describing electronic state
 145 population transition from state i to j (note $P_{ij} \neq P_{ji}^*$). More explicitly, the diagonal elements
 146 of the density matrix ($D_{ii} = 2P_{ii}$) evolves as:⁵⁰

$$\begin{aligned} \frac{\partial}{\partial t} P_{ii} = & -\text{Re}(i[V, P]_{ii}) \quad (2) \\ & + \sum_j \text{Re}(iP_{ij}V_{ji}) f_{ij} (e^{-|\Delta\epsilon_{ij}|^\beta} - 1) \\ & - \sum_j \text{Re}(iP_{ji}V_{ij}) (1 - f_{ij}) (e^{-|\Delta\epsilon_{ij}|^\beta} - 1), \end{aligned}$$

147 while the off-diagonal element of P evolves as:

$$\frac{\partial}{\partial t} P_{ij} = -i [V, P]_{ij} - iV_{ij} (P_{ii} + P_{jj}^*) - \frac{P_{ij}}{\tau_{ij}} \quad (3)$$

148 $\Delta\epsilon_{ij} = \epsilon_i - \epsilon_j$, and $f_{ij} = 1$ (0) for $\Delta\epsilon_{ij} > 0$ and $f_{ij} = 0$ (1) for $\Delta\epsilon_{ij} < 0$ for an electron (hole) dynam-
 149 ics. The last two terms in equation 2 introduce the detailed balance, while the last term in
 150 equation 3 introduces the decoherence. For details of the derivation, we refer to our previous
 151 publications.^{50,51} Combining with CPA, a ground state BOMD simulation is first executed.
 152 During such simulation, it yields the adiabatic eigen state and eigen energy pairs at MD step

153 T_n as $\{\phi_i(T_n), \epsilon_i(T_n)\}$. The overlapping matrix $S_{ij}(T_n, T_{n+1}) = \langle \phi_i(T_n) | \phi_j(T_{n+1}) \rangle$ is recorded.
 154 Here the time step dT of BOMD simulation ($dT = T_{n+1} - T_n$) is around 1 or 2 fs. With the
 155 overlapping matrix, using the eigen state $\{\phi_i(T_n)\}$ as the basis set, the Kohn-Sham Hamilto-
 156 nian at time T_n is: $H_{ij}(T_n) = \epsilon_i(T_n)\delta_{ij}$, while the Hamiltonian at next MD time step T_{n+1} with
 157 the *same* basis $\{\phi_i(T_n)\}$ becomes: $H_{ij}(T_{n+1}) = \sum_k S_{ij}(T_n, T_{n+1})\epsilon_k(T_{n+1})S_{ij}^*(T_n, T_{n+1})$. Here
 158 we assume $S_{ij}(T_n, T_{n+1})$ is a unitary matrix. In practice, a Gram-Schmidt approximation
 159 is used to enforce its unitarity. Knowing $H_{ij}(T_n)$ and $H_{ij}(T_{n+1})$ allows us to linearly inter-
 160 polate the Hamiltonian $H_{ij}(t)$ at any time t within the interval $[T_n, T_{n+1}]$. This effectively
 161 reduces the original plane wave Hamiltonian to a small $N \times N$ Hamiltonian, where N is the
 162 number of $\phi_i(T_n)$ kept in the basis set.⁵¹ To evolve the carrier dynamics following equation
 163 2 and 3, a small time step dt is used from T_n to T_{n+1} . Thus, $H_{ij}(t)$ matrix is diagonalized at
 164 every dt step between T_n and T_{n+1} to get its adiabatic states $\phi_i(t)$ under the basis of $\phi_i(T_n)$,
 165 and $\phi_i(t)$ is used to evaluate $V_{ij}(t)$. In our system, N is more than 300. In practice, it is
 166 still a challenge to integrate $\mathbf{P}(t)$ from T_n to T_{n+1} at every dt step following equation 2 and
 167 3. This is because a small dt is needed due to the possible sharp peaks in evaluating $V_{ij}(t)$
 168 caused by the derivative $\partial\phi_j(t)/\partial t$. This happens when two $\phi_j(t)$ states cross each other,
 169 thus their identities exchanged. Such small dt can result in several thousand steps between
 170 T_n and T_{n+1} . Since each t step requires a $N \times N$ matrix diagonalization of $H_{ij}(t)$ to get $\phi_i(t)$
 171 to evaluate $V_{ij}(t)$, this can be quite expensive. For a complex system with several hundreds
 172 adiabatic states like the interfacial system we are studying, the NAMD simulation can take
 173 days even to accomplish a few MD steps.

174 To solve this problem, in the current study, we have modified the implementation of
 175 NAMD. Instead of diagonalizing the Hamiltonian every dt step from T_n to T_{n+1} , we split
 176 $dT = T_{n+1} - T_n$ into M time-intervals with equal length $\delta t = dT/M$ (M is around 100 and δt
 177 is in the order of 0.01 fs). The start of each time-interval is labeled as t_m (thus $t_m = T_n + m\delta t$)
 178 with $m = 0, 1, \dots, M$. In the modified NAMD, during one δt time-interval from t_m to t_{m+1} ,
 179 instead of using $V_{ij}(t)$, the \mathbf{P} matrix will be evolved using a fixed basis set $\phi_i(t_m)$ which

180 is the adiabatic eigen state obtained at time t_m . The corresponding equation is equation 4.
 181 From t_m to t_{m+1} , there is no need for matrix diagonalization, and $\mathbf{H}(t)$ is obtained from
 182 interpolation under the basis $\phi_i(t_m)$. The diagonalization of the Hamiltonian is only needed
 183 at the start of each time-interval (t_m) to obtain the basis $\phi_i(t_m)$. In this way, the number
 184 of diagonalization operations can be reduced from several thousands to only 100 within one
 185 MD step dT . More specifically, we have:

$$\frac{\partial}{\partial t} P_{ij,m}(t) = -i [H_m(t), P_m(t)]_{ij}. \quad (4)$$

186 for $t \in [t_m, t_{m+1}]$. Here, $\mathbf{H}_m(t)$, $\mathbf{P}_m(t)$ mean the matrix under the basis of $\phi_i(t_m)$. Thus,
 187 if we have solved $\phi_i(t_m) = \sum_j S_{ij}(T_n, t_m) \phi_j(T_n)$ ($\mathbf{S}_m(T_n, t_m)$ is the eigen-vector of the diag-
 188 onalization performed at time t_m), $\mathbf{H}_m(t) = \mathbf{S}(T_n, t_m) \mathbf{H}_{T_n}(t) \mathbf{S}^*(T_n, t_m)$, and $\mathbf{H}_{T_n}(t)$ is the
 189 interpolated Hamiltonian under $\phi_i(T_n)$ basis. To evolve equation 4 from t_m to t_{m+1} , not only
 190 one does not to diagonalize the Hamiltonian, there is also no sharp peaks to $\mathbf{H}_m(t)$. It makes
 191 the time evolution relatively easy. At time t_{m+1} , one diagonalizes the $\mathbf{H}_{T_n}(t_{m+1})$ to obtain
 192 $\phi_i(t_{m+1})$, then converts $\mathbf{P}_m(t_{m+1})$ to $\mathbf{P}'_{m+1}(t_{m+1}) = \mathbf{S}(t_m, t_{m+1}) \mathbf{P}_m(t_{m+1}) \mathbf{S}^*(t_m, t_{m+1})$. Here,
 193 $S_{ij}(t_m, t_{m+1}) = \langle \phi_i(t_m) | \phi_j(t_{m+1}) \rangle$. After this step, the decoherence and detailed balance can
 194 be added as:

$$P_{ii,m+1}(t_{m+1}) = P'_{ii,m+1}(t_{m+1}) + \sum_j \text{Re} [\langle \phi_j(t_m) | \phi_i(t_{m+1}) \rangle P'_{ij,m+1}(t_{m+1})] f_{ij} (e^{-|\Delta\epsilon_{ij}|^\beta} - 1) \quad (5)$$

$$- \sum_j \text{Re} [\langle \phi_i(t_m) | \phi_j(t_{m+1}) \rangle P'_{ji,m+1}(t_{m+1})] (1 - f_{ij}) (e^{-|\Delta\epsilon_{ij}|^\beta} - 1)$$

195 for diagonal element of P_{ii} , and

$$\begin{aligned}
P_{ij,m+1}(t_{m+1}) &= P'_{ij,m+1}(t_{m+1}) \\
&- \langle \phi_i(t_m) | \phi_j(t_{m+1}) \rangle P'_{ii,m+1}(t_{m+1}) + \langle \phi_i(t_{m+1}) | \phi_j(t_m) \rangle P'_{jj,m+1}^*(t_{m+1}) \\
&- P'_{ij,m+1}(t_{m+1}) \frac{t_{m+1} - t_m}{\tau_{ij}}
\end{aligned} \tag{6}$$

196 for off-diagonal elements P_{ij} ($i \neq j$). Such $\mathbf{P}_{m+1}(t_{m+1})$ will be the starting point for the
197 next $[t_{m+1}, t_{m+2}]$ interval calculation using equation 4. Note, in equation 5 and 6, the
198 $\langle \phi_i(t_m) | \phi_j(t_{m+1}) \rangle$ term is used to approximate $V_{ij} \cdot (t_{m+1} - t_m)$ term in equation 2 and 3.
199 To evaluate equation 4 from t_m to t_{m+1} , high order expansion of $e^{i\mathbf{H}dt}$ can be used. How-
200 ever, we find higher orders give negligible improvement over the first-order formalism. The
201 equation 4-6 are approximations of equation 2 and 3. In reality, our test shows that the
202 results using equation 4-6 are almost indistinguishable from the results by equation 2 and
203 3, although the new equations can be hundreds of times faster if large basis set N is used.
204 From the density matrix \mathbf{D} , the charge density of system at time t can be computed as
205 $\rho(\mathbf{r}, t) = \sum_{ij} D_{ij}(t) \phi_i^*(\mathbf{r}, t) \phi_j(\mathbf{r}, t)$. All the NAMD simulations shown below are tested to
206 converge over dt used in equation 4 (dt is set to be 0.0005 fs) and the number of diagonal-
207 izations (value of M) between two MD steps is 100. Although *ab initio* MD takes days, the
208 post-processing NAMD only requires a few hours.

209 We choose one of the adiabatic eigen states characterized by Au d -states as the initial
210 position of the hot hole. For all the NAMD simulations, the initial state is chosen so that
211 more than 85% charges are on Au (see SI Fig.1 for one example). Fig. 2a shows evolution of
212 the energy and the occupation density (defined as $D_{\text{occ}}(E, t) = \sum_i D_{ii}(t) \delta(E - \epsilon_i(t))$) changing
213 with time starting from the initial state. Combining the Fig. 2a with the density of states
214 in Fig. 1b, the whole process can be splitted into three periods: period 1 (from initial hole
215 to around -3.2 eV) possesses the highest hole cooling rate. This is due to the high density
216 of states from both GaN p - and Au d -states. The density of states reduces during period

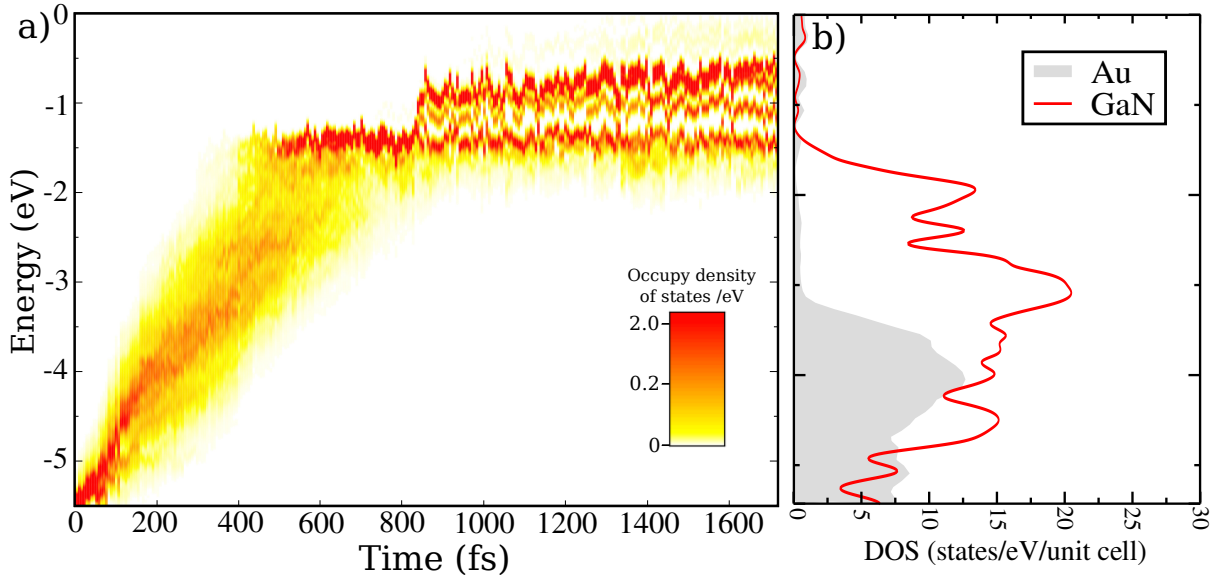


Figure 2: a) Eigen energy of the adiabatic states and their occupation. The color indicates the occupy density of states ($D_{occ}(E, t) = \sum_i D_{ii}(t)\delta(E - \epsilon_i(t))$) for the excited hole. b) Density of states of the structure at time=0 (same to Fig. 1b). The Fermi energy is set at energy zero.

217 2 (from -3.2 eV to -1.5 eV) because of the low density of states of Au contributed by only
 218 its *s*-orbital in this energy range. However, once the hole cools to the edge of GaN valence
 219 bands around 500 fs, the sudden reduction of density of states with only Au *s*-states slows
 220 down the carrier cooling significantly in period 3 (from -1.5 eV to Fermi energy at 0 eV).
 221 Particularly, the relatively sparcity of the Au eigen states within the GaN band gap may
 222 prevent the carrier from cooling to the Fermi energy within our simulation time due to the
 223 phonon bottleneck effect. Since a single-phonon energy is not high enough to satisfy the
 224 energy conservation between different electronic states, the carrier has to wait for a long
 225 time for a multi-phonon scattering process to jump to lower energy states. We have tested
 226 the simulation up to 4 ps, the occupation of the carrier near the Fermi level is still not
 227 significant at the end of the simulation. In the above simulation, the initial energy of the
 228 hot hole relative to Fermi energy is relatively low compared to the typical laser energy used
 229 to excite the plasmon. However, we have also calculated several cases with different initial

230 energies of the hole (all starting from Au *d*-state), they all show similar cooling rate and
231 pathways (SI Fig. 3).

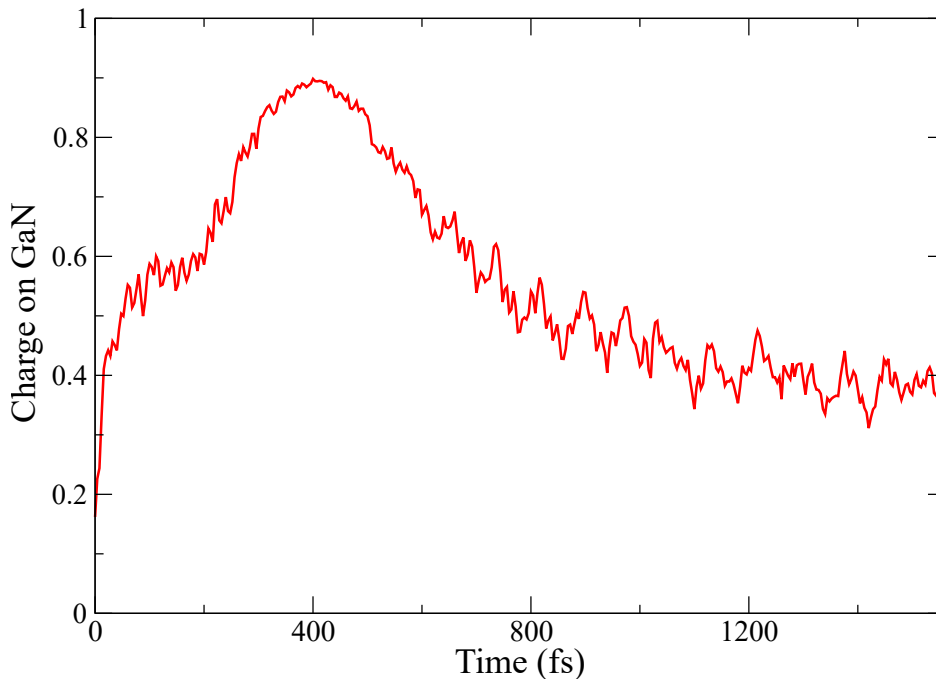


Figure 3: Charge on GaN along with time. The red line is averaged over 20 trajectories. When the charge is counted, charges below the middle line of bottom layer of Au and top layer of GaN are counted as the charge of GaN; otherwise as the charge of Au.

232 In addition to the above energy analysis for the hole's motion, it is possible to analyze
233 its spatial transfer pathways across the interface. In a way, this is already partially shown
234 in Fig. 2, since the density of states (Fig. 2b) illustrates the dominant character of the
235 eigen states within an energy range as GaN, Au or their mix. Fig. 3 shows the charge
236 distributed on GaN as a function of time in a more direct way. Here, we have simulated
237 20 different initial configurations. The curve is the averaged charge distribution over these
238 20 simulations. Note, each P-matrix simulation already includes an ensemble of trajectories
239 starting with the same initial wave function and with the same nuclear trajectory. At the
240 starting point, the majority of the hole-charges are on Au as aforementioned. However, these
241 charges quickly expand to GaN to 50% GaN-occupation within 50 fs. Such fast process is
242 also consistent to previous theoretical investigations.^{41,42} From 50 fs to around 200 fs, the

243 occupation of charge on GaN is a rough plateau around 55%. Together with Fig. 2, we find
 244 that this period corresponds to the carrier cooling within the Au d -state until it reaches the
 245 bottom of d -state (period 1). The 55% occupation may be due to similar density of states
 246 between GaN and Au in this energy region (Fig. 2b). Using a larger Au nanocluster will
 247 shorten this period. This can be observed in the simulation of a 60-Au nanocluster shown
 248 in SI Fig. 5, where the net increase of the density of states caused by larger Au cluster
 249 reduces the “plateau” time but also decreases the distribution of charge in GaN during this
 250 plateau. After 200 fs in Fig. 3, the hot hole begins to transfer to GaN, and nearly 90%
 251 of the hole is inside GaN at around 400 fs. Referring back to Fig. 2a and 2b, one can
 252 see that starting from around 300fs, at the hot carrier’s energy region, the Au only has
 253 its s -state density of states, and the majority of the density of states comes from GaN. At
 254 around 400 fs, the carrier reaches the top of the valence state in GaN, and the maximum
 255 occupation in GaN is also reached. After 400 fs, the occupation inside GaN begins to reduce,
 256 indicating a back-flow to Au for it to reach the Fermi energy in Au. Overall, our simulation
 257 demonstrates that the *majority* of the hot hole tends to cross the interface quickly instead
 258 of waiting inside Au until it has cooled down to the edge of d -state and all the way to the
 259 Fermi energy. The carrier immediately spreads out to GaN before it is cooled down to the
 260 bottom of Au- d states. Although Au nanocluster is only weakly binded to GaN, the vdW
 261 nature of the interaction does not prevent the hole-charge from jumping from Au to GaN.
 262 One might wonder whether this fast spread of carrier localization is due to the small size of
 263 the simulated Au cluster, which might be difficult to contain the carrier wavefunctions (SI
 264 Fig. 1a). But the similar behavior is observed when we increase the Au nanocluster size
 265 from 30 to 60 atoms. As shown in SI Fig. 5, the Au 60-atom case is much alike the Au
 266 30-atom case. Nevertheless, we do see some differences. First, the maximum transfer charge
 267 to GaN has reduced slightly from 90% to 85%, and the charge plateau before the carrier
 268 reaches the top of Au- d states has also reduced from about 55% to 45%. But note that all
 269 these reduction is not inversely proportional to the Au nanocluster size, which has doubled

270 from 30 atoms to 60 atoms. Comparing Fig. 3 with SI Fig. 5, the biggest difference comes
 271 from the time to reach the maximum. Roughly, the cooling rate in the Au 60-atom case is
 272 twice as fast as the case in Au 30-atom case. This means that small Au 30-atom nanocluster
 273 suffers strongly from its phonon-bottleneck effect, and the electron-phonon coupling inside
 274 the Au nanocluster dominates the initial cooling process, despite the fact more than half of
 275 the carrier wavefunction is outside the Au nanocluster.

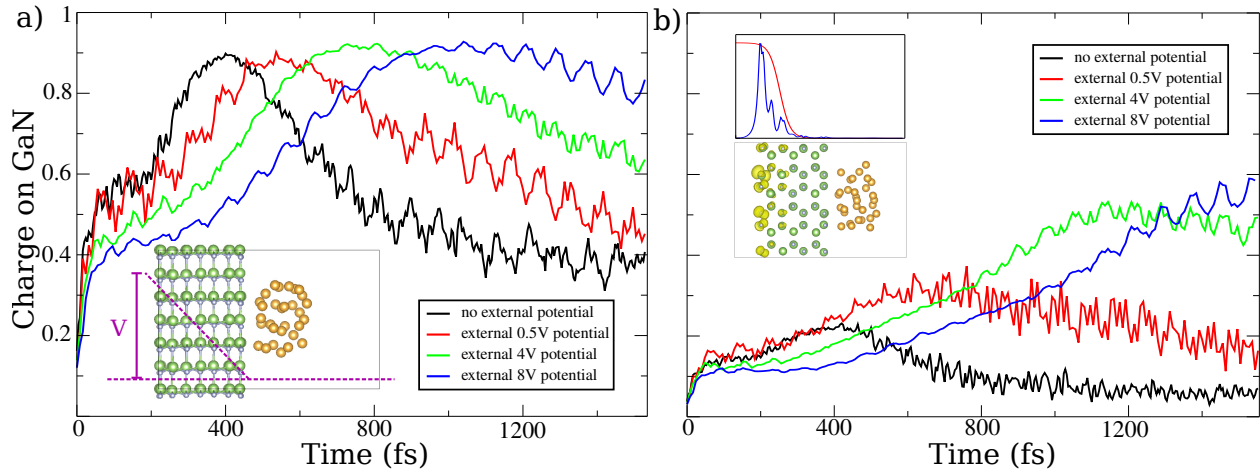


Figure 4: a) Total hole charge in GaN under different external potentials. Inset: the scheme of the applied external potential. b) Charge occupation in the mask region under different external potentials. Inset: (bottom) localized charge density of one adiabatic state under the external potential of 8V, (top) its charge density averaged in $x-y$ plane (blue curve), and the mask function (red curve). To simplify the analysis, charges below the middle line between bottom layer of Au and top layer of GaN are treated belonging to GaN; otherwise they will be counted as charge of Au.

276 After the majority of the hole are transferred to GaN, we observe that some holes return
 277 back to Au after they cool down to the valence band edge of GaN. In Fig. 3, the hole
 278 distribution on GaN starts to decrease to only around 40% from 400 fs up to 1200 fs. It
 279 shows that less than half of the holes stay on GaN, but other holes return back to Au.
 280 Such back transfer has been observed in previous experimental and theoretical works.^{22,40,42}
 281 Particularly, the nonlinear optical technique reveals the returning of the transferred electron
 282 is on picosecond time scale,²² closing to the time of the hole's returning in our calculation.
 283 Thus, it is something to be prevented since it reduces the eventual carrier harvesting. It

284 will be quite useful to engineer the interface to reduce this back transfer. Before we discuss
285 different ways to mitigate this back flow, it is worth to discuss first the possible artifacts
286 which contribute to this back flow. In a real system, when the charge is transferred out of
287 Au, it can move into the bulk of GaN far away from Au nanocluster, thus never returns. To
288 show the back flow due to the finite size of the system, we perform a simulation of the same
289 system but putting the initial hole in the GaN above the d -state of Au (see SI). We find that
290 the “warm” hole (its energy is above the Au d -state) spreads from GaN to Au in very similar
291 fashion as the back transfer case shown in Fig.3 (SI Fig.4). Our calculation demonstrates
292 that the back flow is non-avoidable given the small GaN layer we can afford. We believe due
293 to the limited GaN layers in our simulation, the effect of back flow is probably overestimated.
294 Nevertheless, we should still be able to design heterostructures to enhance the hole transfer
295 to GaN, as the qualitative trend should still be the same. The relative values of the back
296 flow to Au should still be a good indicator.

297 The experiments of the heterostructure Au/p-type GaN illustrated in Ref. 16 and 23
298 demonstrate the hole harvesting from Au to GaN. The Schottky-barrier band bending in
299 this system has been shown to play a central role to assist the hole transfer. The careful
300 design of such heterostructure allows the formation of the internal electric field near the
301 interface resulting from the band bending in the depletion layers. Such electric field can
302 drive the hole away and reduce their back transfer. In order to demonstrate the role of
303 the internal electric field, we perform MD and NAMD simulations under different external
304 electric fields. Shown in Fig. 4a inset is the scheme of the external potentials added to
305 mimic the Schottky barrier band bending. External potentials with values of 0.5V, 4V and
306 8V at the vacuum side end of GaN are applied linearly inside GaN, respectively. For all
307 these cases, the states near the Fermi energy are still Au states. Thus, thermodynamically,
308 the hole should still return to Au. Fig. 4a shows the spatial charge occupation on GaN as a
309 function of time under different external potentials. It is interesting to see that by applying
310 higher electric field, more holes tend to stay on GaN for a longer time, less likely to return to

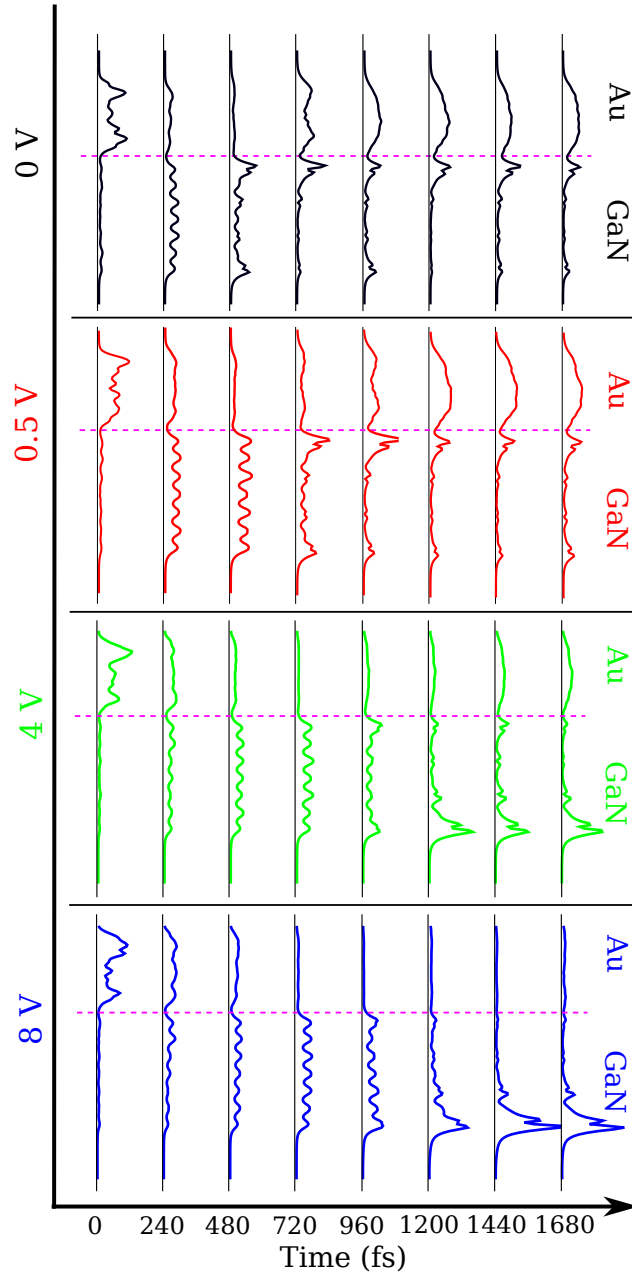


Figure 5: Charge density evolution with time under different external potentials (from top to bottom, 0V, 0.5V, 4V and 8V). Dashed magenta line separate Au and GaN regions. The charge density is averaged in $x - y$ plane of the simulation cell as $\rho(z; t) = \int \rho(x, y, z; t) dx dy$.

311 Au. Even a relatively low external potential of 0.5V can affect the behaviour of the excited
 312 hole noticeably. It is also interesting to see that the time of the charges arriving at GaN also
 313 becomes slower when the field strength increases. This is due to a shift of GaN density of
 314 state. The lack of density of states at higher electric field reduces the initial charge transfer
 315 rate. In order to further understand the charge distribution inside GaN. Fig. 4b illustrates
 316 the charge distribution of the localized adiabatic state within a “mask” region at the end
 317 of GaN in its vacuum side as shown in the inset. We use a mask function to capture such
 318 state. This mask $m(\mathbf{r})$ is then used to calculate $\int \rho(\mathbf{r}, t)m(\mathbf{r})d^3\mathbf{r}$, and the result is shown
 319 in Fig. 4b. As we have discussed above, our calculation may overestimate the amount of
 320 the charge returning to Au and have almost 100% return of the charge to Au if the running
 321 of our calculation is infinitely long, since the states at Fermi energy is localized inside Au.
 322 It is thus helpful if we can define a measure of charge density inside GaN, and assume the
 323 measured charge to disappear into the bulk of GaN in an infinite GaN system. One such
 324 measure is the trapped charge within that mask. It is reasonable to assume that once the
 325 charge is “trapped” in this mask region, it can be considered as going to the bulk GaN, and
 326 never returns. Thus, we can use the highest amplitude of the charge inside the mask region
 327 during the simulation time to provide a quantitative measure of the total charge captured by
 328 the bulk GaN. The subsequent decay of the charge within the mask region is due to the back
 329 flow to higher energy Au state owing to the finite size of the simulated system. Note, this is
 330 probably a lower-limit estimation, since before it reaches the maximum, some of the charge
 331 might already return to the Au due to the finite GaN size (hence once again, overestimation
 332 of the back flow). Besides, the mask function itself only calculates the state near the end of
 333 GaN, thus can miss other states of GaN. Nevertheless, we can use these numbers to provide
 334 an estimate. Under the external potentials of 0, 0.5, 4, and 8V, we get the maximum charge
 335 of 22%, 35%, 50% and 60%, respectively.

336 To further understand the details of the charge distribution in real space, Fig. 5 illustrates
 337 the charge density chosen from one initial state run averaged over x - y plane under different

338 external potentials (from top to bottom: 0V, 0.5V, 4V and 8V) as a function of time.
 339 All the cases show a sub-picosecond fast charge transfer from Au to GaN. For 0 V, the
 340 charges on GaN never stay significantly in the mask region. For 0.5 V case, there is a
 341 slight distribution in this region, but most of the charge escapes to Au eventually. When
 342 the electric field increases further, the mask regions start to be populated clearly after the
 343 charges are transferred to GaN, indicating the efficiency of the band bending to assist the
 344 hole transfer in Au/GaN heterostructure.

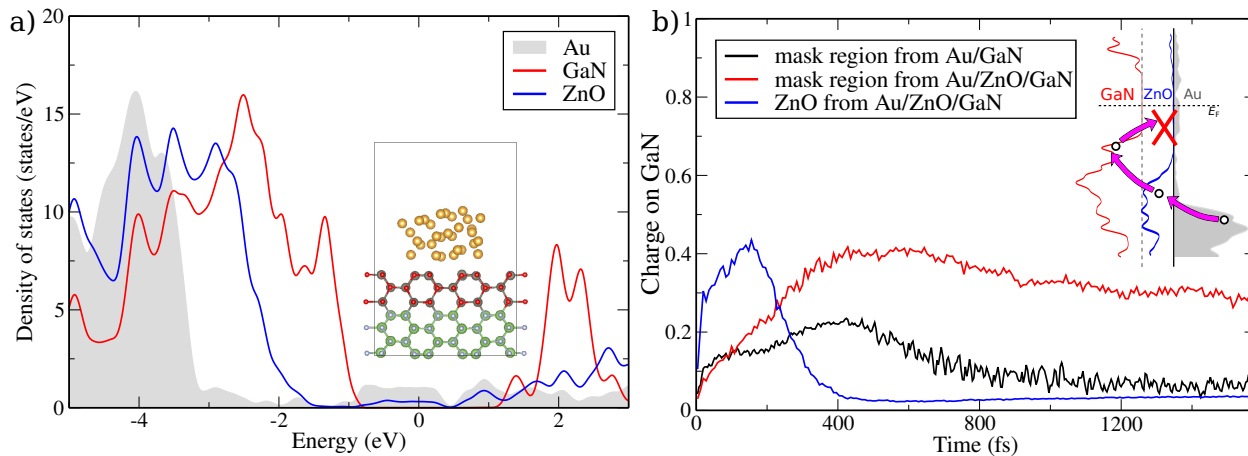


Figure 6: a) The projected density of states of Au, ZnO and GaN. Inset: relaxed structure of Au/ZnO/GaN heterostructure at 0K (Red: oxygen atom, Dark grey: zinc atom). b) The charge distribution of GaN and ZnO compared to the pure Au/GaN system. The mask region is the same to the pure Au/GaN case (Fig. 4b). Inset: illustration of the role of ZnO in preventing the hole from returning back to Au after it reaches the band edge of GaN. But the initial hot hole transfer from Au to GaN is not affected by ZnO.

345 In addition to the Schottky barrier and its induced internal electric field, following our
 346 understanding of the charge back flow, we propose to use a hole-block layer to prevent the
 347 back flow. Such inserted layer separates GaN and Au wavefunction spatially to reduce their
 348 coupling, hence to prevent the back flow of the equilibrated hole carrier. On the other hand,
 349 the inserted layer should have a potential barrier low enough so that it will not block the
 350 initial hot carrier transfer from Au to GaN. We find ZnO is a good choice. Similar to
 351 GaN, ZnO possesses wide band gap. Its valence band maximum is around 0.8 eV lower
 352 than that of GaN, roughly at the same level of *d*-states edge of Au.⁵⁸ Interestingly, ZnO

353 has quite similar structure (Wurtzite crystal shape) and lattice constants to GaN, which
354 brings a great advantage for high quality synthesis as well as theoretical simulation. In our
355 calculation, we replace top three layers of GaN by ZnO (Fig. 6a inset), relax the whole
356 structure, and compute the projection of the density of states. Fig. 6a shows the position
357 of the ZnO states, which is consistent to the experiments.^{57,58,62,63} By performing MD and
358 post-processing NAMD simulations, the time-dependent spatial charge distribution on GaN
359 is obtained, and shown in Fig. 6b. Similar to the case of Au/GaN, the hot hole transfers
360 to GaN by passing through ZnO. This initial charge transfer is not significantly reduced
361 by the existence of ZnO. After the charge reaches the band edge of GaN and becomes an
362 equilibrium “cold” carrier, the potential created by ZnO effectively reduces the coupling
363 between GaN and Au, and diminishes the back flow to Au. Using the same approach as
364 for the external potential case, we obtain the maximum amount of charge transfer in the
365 mask region. We get a value of more than 40%, which is much higher than the 22% of the
366 pure Au/GaN structure. The effect of the three layer of ZnO is equivalent to an applied
367 external potential between 0.5 and 4V. Furthermore, when the amount of charges inside the
368 mask region reaches the maximum, its subsequent reduction also becomes slower compared
369 to pure Au/GaN case even with an external potential. It further shows the effectiveness of
370 ZnO layer lowering the back flow from GaN to Au.

371 In summary, we have performed a detailed hot hole dynamics with quantum mechanics
372 non-adiabatic molecular dynamics simulation for the heterostructure Au/GaN. By setting
373 up the hole initially at Au *d*-state, the *ab initio* MD and the post-processing NAMD reveal
374 that the time-scale for the hole transfer is less than 200 fs. The excited hole first cools to
375 the band edge of Au *d*-state, while at the mean time spread out into GaN. The majority of
376 the charge then quickly cool down further to the edge of GaN. We also observe that some
377 of the charge can return back to Au after it reaches the band edge of GaN. To understand
378 the role of band bending in Schottky barrier, different external potentials are applied. The
379 NAMD simulation shows that the internal electric field can indeed enhance the hole transfer

380 from Au to GaN. Using a special technique of GaN edge trapping state, we estimate the
381 lower limit of total charge transfer amplitude when the external potential is 0, 0.5, 4 and 8V,
382 as 22%, 35%, 50% and 60%, respectively. We also propose a ZnO insertion layer between
383 GaN and Au to prevent the back flow of the “cold” hole, while keep the initial hot carrier
384 flowing from Au to GaN. We find more than 40% electron transfer to GaN when ZnO layer
385 is used, this is to compare with the 22% electron transfer without the ZnO hole-block layer.
386 Finally, we also find that increasing the Au nanocluster from 30-atom to 60-atom will speed
387 up the hot carrier cooling rate significantly, but only slightly reduce the hot carrier transfer
388 amplitude from Au to GaN. This indicates that the cooling is predominately caused by the
389 electron-phonon coupling within Au, and the phonon bottleneck plays an important role.
390 Our calculation demonstrates that the newly developed P-matrix method can be used to
391 study carrier dynamics for systems with hundreds of atoms, and to simulate the dynamics
392 for multiple picoseconds.

393 **Acknowledgement**

394 This material is based on the work performed by the Joint Center for Artificial Photosyn-
395 thesis, a DOE Energy Innovation Hub, supported through the Office of Science of the U.S.
396 Department of Energy under Award number DE-SC0004993. We use the resource of National
397 Energy Research Scientific Computing center (NERSC) located in Lawrence Berkeley Na-
398 tional Laboratory and the computational resource of the Oak Ridge Leadership Computing
399 Facility at the Oak Ridge National Laboratory under the Innovative and Novel Computa-
400 tional Impact on Theory and Experiment project.

401 **References**

- 402 (1) Mukherjee, S.; Libisch, F.; Large, N.; Neumann, O.; Brown, L. V.; Cheng, J.; Las-
403 siter, J. B.; Carter, E. A.; Nordlander, P.; Halas, N. J. Hot Electrons Do the Impossible:

- 404 Plasmon-Induced Dissociation of H₂ on Au. *Nano Letters* **2013**, *13*, 240–247.
- 405 (2) Moskovits, M. The Case for Plasmon-Derived Hot Carrier Devices. *Nature Nanotech-*
406 *nology* **2015**, *10*, 6–8.
- 407 (3) Clavero, C. Plasmon-Induced Hot-Electron Generation at Nanoparticle/Metal-Oxide
408 Interfaces for Photovoltaic and Photocatalytic Devices. *Nature Photonics* **2014**, *8*, 95–
409 103.
- 410 (4) Christopher, P.; Moskovits, M. Hot Charge Carrier Transmission from Plasmonic
411 Nanostructures. *Annual Review of Physical Chemistry* **2017**, *68*, 379–398.
- 412 (5) Ma, J.; Wang, Z.; Wang, L.-W. Interplay between Plasmon and Single-Particle Excita-
413 tions in a Metal Nanocluster. *Nature Communications* **2015**, *6*, 10107.
- 414 (6) Robotjazi, H.; Bahauddin, S. M.; Doiron, C.; Thomann, I. Direct Plasmon-Driven
415 Photoelectrocatalysis. *Nano Letters* **2015**, *15*, 6155–6161.
- 416 (7) Zhong, Y.; Ueno, K.; Mori, Y.; Shi, X.; Oshikiri, T.; Murakoshi, K.; Inoue, H.; Mi-
417 sawa, H. Plasmon-Assisted Water Splitting Using Two Sides of the Same SrTiO₃
418 Single-Crystal Substrate: Conversion of Visible Light to Chemical Energy. *Angewandte*
419 *Chemie International Edition* **2014**, *53*, 10350–10354.
- 420 (8) Mubeen, S.; Lee, J.; Singh, N.; Krämer, S.; Stucky, G. D.; Moskovits, M. An Au-
421 tonomous Photosynthetic Device in Which All Charge Carriers Derive from Surface
422 Plasmons. *Nature Nanotechnology* **2013**, *8*, 247–251.
- 423 (9) Marimuthu, A.; Zhang, J.; Linic, S. Tuning Selectivity in Propylene Epoxidation by
424 Plasmon Mediated Photo-Switching of Cu Oxidation State. *Science* **2013**, *339*, 1590–
425 1593.
- 426 (10) Christopher, P.; Xin, H.; Linic, S. Visible-Light-Enhanced Catalytic Oxidation Reac-
427 tions on Plasmonic Silver Nanostructures. *Nature Chemistry* **2011**, *3*, 467–472.

- 428 (11) Wu, B.; Liu, D.; Mubeen, S.; Chuong, T. T.; Moskovits, M.; Stucky, G. D. Anisotropic
429 Growth of TiO₂ onto Gold Nanorods for Plasmon-Enhanced Hydrogen Production from
430 Water Reduction. *Journal of the American Chemical Society* **2016**, *138*, 1114–1117.
- 431 (12) Zhou, L.; Zhang, C.; McClain, M. J.; Manjavacas, A.; Krauter, C. M.; Tian, S.; Berg, F.;
432 Everitt, H. O.; Carter, E. A.; Nordlander, P.; Halas, N. J. Aluminum Nanocrystals as
433 a Plasmonic Photocatalyst for Hydrogen Dissociation. *Nano Letters* **2016**, *16*, 1478–
434 1484.
- 435 (13) Mukherjee, S.; Zhou, L.; Goodman, A. M.; Large, N.; Ayala-Orozco, C.; Zhang, Y.;
436 Nordlander, P.; Halas, N. J. Hot-Electron-Induced Dissociation of H₂ on Gold Nanopar-
437 ticles Supported on SiO₂. *Journal of the American Chemical Society* **2014**, *136*, 64–67.
- 438 (14) Mubeen, S.; Lee, J.; Liu, D.; Stucky, G. D.; Moskovits, M. Panchromatic Photoproduc-
439 tion of H₂ with Surface Plasmons. *Nano Letters* **2015**, *15*, 2132–2136.
- 440 (15) Robotjazi, H.; Zhao, H.; Swearer, D. F.; Hogan, N. J.; Zhou, L.; Alabastri, A.; Mc-
441 Clain, M. J.; Nordlander, P.; Halas, N. J. Plasmon-Induced Selective Carbon Dioxide
442 Conversion on Earth-Abundant Aluminum-Cuprous Oxide Antenna-Reactor Nanopar-
443 ticles. *Nature Communications* **2017**, *8*, 27.
- 444 (16) DuChene, J. S.; Tagliabue, G.; Welch, A. J.; Cheng, W.-H.; Atwater, H. A. Hot Hole
445 Collection and Photoelectrochemical CO₂ Reduction with Plasmonic Au/p-GaN Pho-
446 tocoathodes. *Nano Letters* **2018**, *18*, 2545–2550.
- 447 (17) Clark, M. L.; Ge, A.; Videla, P. E.; Rudshiteyn, B.; Miller, C. J.; Song, J.; Batista, V. S.;
448 Lian, T.; Kubiak, C. P. CO₂ Reduction Catalysts on Gold Electrode Surfaces Influenced
449 by Large Electric Fields. *Journal of the American Chemical Society* **2018**, *140*, 17643–
450 17655.
- 451 (18) Li, J.; Cushing, S. K.; Zheng, P.; Senty, T.; Meng, F.; Bristow, A. D.; Manivannan, A.;
452 Wu, N. Solar Hydrogen Generation by a CdS-Au-TiO₂ Sandwich Nanorod Array En-

- 453 hanced with Au Nanoparticle as Electron Relay and Plasmonic Photosensitizer. *Journal*
454 *of the American Chemical Society* **2014**, *136*, 8438–8449.
- 455 (19) Furube, A.; Du, L.; Hara, K.; Katoh, R.; Tachiya, M. Ultrafast Plasmon-Induced Elec-
456 tron Transfer from Gold Nanodots into TiO₂ Nanoparticles. *Journal of the American*
457 *Chemical Society* **2007**, *129*, 14852–14853.
- 458 (20) Tian, Y.; Tatsuma, T. Mechanisms and Applications of Plasmon-Induced Charge Sepa-
459 ration at TiO₂ Films Loaded with Gold Nanoparticles. *Journal of the American Chem-*
460 *ical Society* **2005**, *127*, 7632–7637.
- 461 (21) Mubeen, S.; Hernandez-Sosa, G.; Moses, D.; Lee, J.; Moskovits, M. Plasmonic Pho-
462 tosensitization of a Wide Band Gap Semiconductor: Converting Plasmons to Charge
463 Carriers. *Nano Letters* **2011**, *11*, 5548–5552.
- 464 (22) Tisdale, W. A.; Williams, K. J.; Timp, B. A.; Norris, D. J.; Aydil, E. S.; Zhu, X.-Y. Hot-
465 Electron Transfer from Semiconductor Nanocrystals. *Science* **2010**, *328*, 1543–1547.
- 466 (23) Tagliabue, G.; DuChene, J. S.; Abdellah, M.; Habib, A.; Hattori, Y.; Zheng, K.; Can-
467 ton, S. E.; Gosztola, D. J.; Cheng, W.-H.; Sá, J.; Atwater, H. A. Ultrafast Studies of
468 Hot-Hole Dynamics in Au/p-GaN Heterostructures. 12.
- 469 (24) Du, L.; Furube, A.; Hara, K.; Katoh, R.; Tachiya, M. Ultrafast Plasmon Induced
470 Electron Injection Mechanism in Gold–TiO₂ Nanoparticle System. *Journal of Photo-*
471 *chemistry and Photobiology C: Photochemistry Reviews* **2013**, *15*, 21–30.
- 472 (25) Wen, X.; Xu, W.; Zhao, W.; Khurgin, J. B.; Xiong, Q. Plasmonic Hot Carriers-
473 Controlled Second Harmonic Generation in WSe₂ Bilayers. *Nano Letters* **2018**, *18*,
474 1686–1692.
- 475 (26) Yu, Y.; Ji, Z.; Zu, S.; Du, B.; Kang, Y.; Li, Z.; Zhou, Z.; Shi, K.; Fang, Z. Ultrafast

- 476 Plasmonic Hot Electron Transfer in Au Nanoantenna/MoS₂ Heterostructures. *Advanced*
477 *Functional Materials* **2016**, *26*, 6394–6401.
- 478 (27) Anderson, N. A.; Lian, T. ULTRAFAST ELECTRON TRANSFER AT THE
479 MOLECULE-SEMICONDUCTOR NANOPARTICLE INTERFACE. *Annual Review*
480 *of Physical Chemistry* **2005**, *56*, 491–519.
- 481 (28) Grimaldi, G.; Crisp, R. W.; ten Brinck, S.; Zapata, F.; van Ouwendorp, M.; Renaud, N.;
482 Kirkwood, N.; Evers, W. H.; Kinge, S.; Infante, I.; Siebbeles, L. D. A.; Houtepen, A. J.
483 Hot-Electron Transfer in Quantum-Dot Heterojunction Films. *Nature Communications*
484 **2018**, *9*, 2310.
- 485 (29) Sundararaman, R.; Narang, P.; Jermyn, A. S.; Goddard Iii, W. A.; Atwater, H. A. The-
486oretical Predictions for Hot-Carrier Generation from Surface Plasmon Decay. *Nature*
487 *Communications* **2014**, *5*, 5788.
- 488 (30) Brown, A. M.; Sundararaman, R.; Narang, P.; Goddard, W. A.; Atwater, H. A. Nonra-
489diative Plasmon Decay and Hot Carrier Dynamics: Effects of Phonons, Surfaces, and
490 Geometry. *ACS Nano* **2016**, *10*, 957–966.
- 491 (31) Govorov, A. O.; Zhang, H.; Gun'ko, Y. K. Theory of Photoinjection of Hot Plasmonic
492 Carriers from Metal Nanostructures into Semiconductors and Surface Molecules. *The*
493 *Journal of Physical Chemistry C* **2013**, *117*, 16616–16631.
- 494 (32) Zhou, J.-J.; Hellman, O.; Bernardi, M. Electron-Phonon Scattering in the Presence of
495 Soft Modes and Electron Mobility in SrTiO₃ Perovskite from First Principles. *Physical*
496 *Review Letters* **2018**, *121*, 226603.
- 497 (33) Bernardi, M.; Vigil-Fowler, D.; Lischner, J.; Neaton, J. B.; Louie, S. G. Ab Initio Study
498 of Hot Carriers in the First Picosecond after Sunlight Absorption in Silicon. *Physical*
499 *Review Letters* **2014**, *112*, 257402.

- 500 (34) Marcus, R. A. On the Theory of Oxidation-Reduction Reactions Involving Electron
501 Transfer. I. *The Journal of Chemical Physics* **1956**, *24*, 966–978.
- 502 (35) Wei, H.; Luo, J.-W.; Li, S.-S.; Wang, L.-W. Revealing the Origin of Fast Electron
503 Transfer in TiO₂-Based Dye-Sensitized Solar Cells. *Journal of the American Chemical*
504 *Society* **2016**, *138*, 8165–8174.
- 505 (36) Liu, Y.-Y.; Zheng, F.; Jiang, X.; Luo, J.-W.; Li, S.-S.; Wang, L.-W. *Ab Initio* Inves-
506 tigation of Charge Trapping Across the Crystalline- Si –Amorphous- Si O₂ Interface.
507 *Physical Review Applied* **2019**, *11*, 044058.
- 508 (37) Tarafder, K.; Surendranath, Y.; Olshansky, J. H.; Alivisatos, A. P.; Wang, L.-W. Hole
509 Transfer Dynamics from a CdSe/CdS Quantum Rod to a Tethered Ferrocene Derivative.
510 *Journal of the American Chemical Society* **2014**, *136*, 5121–5131.
- 511 (38) Chu, I.-H.; Radulaski, M.; Vukmirovic, N.; Cheng, H.-P.; Wang, L.-W. Charge Trans-
512 port in a Quantum Dot Supercrystal. *The Journal of Physical Chemistry C* **2011**, *115*,
513 21409–21415.
- 514 (39) Duncan, W. R.; Craig, C. F.; Prezhdo, O. V. Time-Domain *Ab Initio* Study of Charge
515 Relaxation and Recombination in Dye-Sensitized TiO₂. *Journal of the American Chem-*
516 *ical Society* **2007**, *129*, 8528–8543.
- 517 (40) Prezhdo, O. V.; Duncan, W. R.; Prezhdo, V. V. Photoinduced Electron Dynamics
518 at the Chromophore–Semiconductor Interface: A Time-Domain *Ab Initio* Perspective.
519 *Progress in Surface Science* **2009**, *84*, 30–68.
- 520 (41) Zhang, J.; Guan, M.; Lischner, J.; Meng, S.; Prezhdo, O. V. Coexistence of Differ-
521 ent Charge-Transfer Mechanisms in the Hot-Carrier Dynamics of Hybrid Plasmonic
522 Nanomaterials. *Nano Letters* **2019**,

- 523 (42) Long, R.; Prezhdo, O. V. Instantaneous Generation of Charge-Separated State on TiO₂
524 Surface Sensitized with Plasmonic Nanoparticles. *Journal of the American Chemical*
525 *Society* **2014**, *136*, 4343–4354.
- 526 (43) Zhang, Z.; Liu, L.; Fang, W.-H.; Long, R.; Tokina, M. V.; Prezhdo, O. V. Plasmon-
527 Mediated Electron Injection from Au Nanorods into MoS₂: Traditional versus Pho-
528 toexcitation Mechanism. *Chem* **2018**, *4*, 1112–1127.
- 529 (44) Long, R.; Prezhdo, O. V. Ab Initio Nonadiabatic Molecular Dynamics of the Ultrafast
530 Electron Injection from a PbSe Quantum Dot into the TiO₂ Surface. *Journal of the*
531 *American Chemical Society* **2011**, *133*, 19240–19249.
- 532 (45) Zhang, J.; Hong, H.; Zhang, J.; Fu, H.; You, P.; Lischner, J.; Liu, K.; Kaxiras, E.;
533 Meng, S. New Pathway for Hot Electron Relaxation in Two-Dimensional Heterostruc-
534 tures. *Nano Letters* **2018**, *18*, 6057–6063.
- 535 (46) Long, R.; English, N. J.; Prezhdo, O. V. Photo-Induced Charge Separation across the
536 Graphene–TiO₂ Interface Is Faster than Energy Losses: A Time-Domain Ab Initio
537 Analysis. *Journal of the American Chemical Society* **2012**, *134*, 14238–14248.
- 538 (47) Zhou, X.; Tokina, M. V.; Tomko, J. A.; Braun, J. L.; Hopkins, P. E.; Prezhdo, O. V.
539 Thin Ti Adhesion Layer Breaks Bottleneck to Hot Hole Relaxation in Au Films. *The*
540 *Journal of Chemical Physics* **2019**, *150*, 184701.
- 541 (48) Nam, Y.; Li, L.; Lee, J. Y.; Prezhdo, O. V. Strong Influence of Oxygen Vacancy Location
542 on Charge Carrier Losses in Reduced TiO₂ Nanoparticles. *The Journal of Physical*
543 *Chemistry Letters* **2019**, *10*, 2676–2683.
- 544 (49) Senanayake, R. D.; Guidez, E. B.; Neukirch, A. J.; Prezhdo, O. V.; Aikens, C. M.
545 Theoretical Investigation of Relaxation Dynamics in Au₃₈(SH)₂₄ Thiolate-Protected
546 Gold Nanoclusters. *The Journal of Physical Chemistry C* **2018**, *122*, 16380–16388.

- 547 (50) Kang, J.; Wang, L.-W. Nonadiabatic Molecular Dynamics with Decoherence and De-
548 tailed Balance under a Density Matrix Ensemble Formalism. *Physical Review B* **2019**,
549 *99*, 224303.
- 550 (51) Ren, J.; Vukmirović, N.; Wang, L.-W. Nonadiabatic Molecular Dynamics Simulation
551 for Carrier Transport in a Pentathiophene Butyric Acid Monolayer. *Physical Review B*
552 **2013**, *87*, 205117.
- 553 (52) Jia, W.; Cao, Z.; Wang, L.; Fu, J.; Chi, X.; Gao, W.; Wang, L.-W. The Analysis of
554 a Plane Wave Pseudopotential Density Functional Theory Code on a GPU Machine.
555 *Computer Physics Communications* **2013**, *184*, 9–18.
- 556 (53) Jia, W.; Fu, J.; Cao, Z.; Wang, L.; Chi, X.; Gao, W.; Wang, L.-W. Fast Plane Wave
557 Density Functional Theory Molecular Dynamics Calculations on Multi-GPU Machines.
558 *Journal of Computational Physics* **2013**, *251*, 102–115.
- 559 (54) Perdew, J. P.; Burke, K.; Ernzerhof, M. Generalized Gradient Approximation Made
560 Simple. *Physical Review Letters* **1996**, *77*, 3865–3868.
- 561 (55) Hamann, D. R. Optimized Norm-Conserving Vanderbilt Pseudopotentials. *Physical Re-*
562 *view B* **2013**, *88*, 085117.
- 563 (56) Fadley, C.; Shirley, D. Electronic Densities of States from X-Ray Photoelectron Spec-
564 troscopy. *Journal of Research of the National Bureau of Standards Section A: Physics*
565 *and Chemistry* **1970**, *74A*, 543.
- 566 (57) Hinuma, Y.; Grüneis, A.; Kresse, G.; Oba, F. Band Alignment of Semiconductors from
567 Density-Functional Theory and Many-Body Perturbation Theory. *Physical Review B*
568 **2014**, *90*.
- 569 (58) Stevanović, V.; Lany, S.; S. Ginley, D.; Tumas, W.; Zunger, A. Assessing Capability

- 570 of Semiconductors to Split Water Using Ionization Potentials and Electron Affinities
571 Only. *Physical Chemistry Chemical Physics* **2014**, *16*, 3706–3714.
- 572 (59) Beach, J. D.; Collins, R. T.; Turner, J. A. Band-Edge Potentials of n-Type and p-Type
573 GaN. *Journal of The Electrochemical Society* **2003**, *150*, A899.
- 574 (60) Singh-Miller, N. E.; Marzari, N. Surface Energies, Work Functions, and Surface Relax-
575 ations of Low-Index Metallic Surfaces from First Principles. *Physical Review B* **2009**,
576 *80*.
- 577 (61) Lymperakis, L.; Neugebauer, J.; Himmerlich, M.; Krischok, S.; Rink, M.; Kröger, J.;
578 Polyakov, V. M. Adsorption and Desorption of Hydrogen at Nonpolar GaN(1-100) Sur-
579 faces: Kinetics and Impact on Surface Vibrational and Electronic Properties. *Physical*
580 *Review B* **2017**, *95*.
- 581 (62) Jacobi, K.; Zwicker, G.; Gutmann, A. Work Function, Electron Affinity and Band
582 Bending of Zinc Oxide Surfaces. *Surface Science* **1984**, *141*, 109–125.
- 583 (63) Matsumoto, Y.; Yoshikawa, T.; Sato, E.-i. Dependence of the Band Bending of the
584 Oxide Semiconductors on pH. *Journal of The Electrochemical Society* **1989**, *136*, 1389–
585 1391.